

---

Wesleyan University

---

# **Exploring the Role of Environment in the Composition of ONC Proplyds**

by

Jonas Powell  
Class of 2019

A thesis submitted to the  
faculty of Wesleyan University  
in partial fulfillment of the requirements for the  
Degree of Master of Arts

---

Middletown, Connecticut

---

April, 2018

---

*If people sat outside and looked at the stars each night,  
I'll bet they'd live a lot differently.*

—CALVIN & HOBBES

---

# Contents

<b>1 Analysis</b>	<b>1</b>
1.1 Gas Model . . . . .	1
1.1.1 Establishing Physical Profiles . . . . .	2
1.1.2 Generating a Model Image . . . . .	5
1.2 Exploring Parameter Space . . . . .	6
1.2.1 Grid Search . . . . .	7
1.2.2 Markov Chain Monte Carlo . . . . .	7
1.3 Fitting Procedure . . . . .	10
1.3.1 HCO <sup>+</sup> (4-3) Fit . . . . .	11
1.3.2 HCN(4-3) Fit . . . . .	13
1.3.3 CO(3-2) Fit . . . . .	16
1.4 Reflections on the Fits . . . . .	17
<b>Bibliography</b>	<b>26</b>

# List of Figures

1.1	Since disk A and B's features are assumed to be independent, we may generate corner plots for each of their parameter spaces individually. Some analysis. REWORK: these are not the most recent ones . . . . .	10
1.2	Moment-1 map of HCN emission, overlaid with ellipses described by each disk's best-fit position angle, inclination, and outer radius. For disk B, both the best-fit outer radius with and without the 220 AU a posteriori prior implemented (at 324 and 145 AU, respectively) are plotted. . . . .	14
1.3	Cornerplots of results from MCMC fitting of $\text{HCO}^+$ emission. . .	19
1.4	Channel maps of $\text{HCO}^+$ emission data, as well as a best-fit model from MCMC fitting and residuals from the two. . . . .	20
1.5	Cornerplots of results from MCMC fitting of HCN emission. . . .	21
1.6	Channel maps of HCN emission data, as well as a best-fit model from MCMC fitting and residuals from the two. . . . .	22
1.7	Cornerplots of results from MCMC fitting of HCN emission. . . .	23
1.8	Channel maps of CO emission data, as well as a best-fit model from MCMC fitting and residuals from the two. . . . .	24
1.9	Density and temperature profiles for the best-fit models for CO, $\text{HCO}^+$ , and HCN. . . . .	25

# Chapter 1

## Analysis

By modeling spatially and spectrally resolved observations of protoplanetary disks, we can measure their chemical and physical characteristics. To model the system, we generate a synthetic image of what a disk with known characteristics (like disk radius, mass, chemical abundances, and so on) would look like at a certain distance, inclination, and position angle relative to us. We can then turn that synthetic image into a synthetic visibility set, and then compare those visibilities to our observations. By iterating this process and varying the value of those input parameters, we are able to generate many models with different parameter combinations, evaluate how well each resulting model disk matches our observations, and find which values best describe our disks.

In §1.1, we describe the basic equations and computational processes that generate the model disks. In §1.2, we describe how, once models are made, we move through high-dimensional parameter space to identify regions of best-fit. Finally, in §1.3, we present the results of our fitting procedures.

### 1.1 Gas Model

In this work, we use a gas disk model originally developed by Rosenfeld et al. (2012, 2013) and translated from IDL to Python by Flaherty et al. (2015). The

code assumes local thermal equilibrium<sup>1</sup> (LTE) and hydrostatic equilibrium. The code draws on temperature and surface density profiles provided by the user to calculate a vertical density structure, and calculates the model disk’s velocity field based on the stellar mass. It then performs radiative transfer on the resulting structure to create a sky-projected image of the model disk, taking into account thermal and turbulent line broadening. The assumption of LTE allows the code to run quickly enough for a Markov Chain Monte Carlo routine to generate models on a reasonable timescale, as described in §1.2.2.

### 1.1.1 Establishing Physical Profiles

A circumstellar disk can be characterized by three major profiles: its radial and vertical temperature structures, its radial and vertical density structures, and its velocity field. Generating a model disk is a matter of defining these three functions.

For the disk’s temperature profile, our code uses the parametrization of disk temperature structure first laid out by Dartois et al. (2003), where the disk’s temperature is given by,

$$T_{\text{gas}}(r, z) = \begin{cases} T_a + (T_m - T_a) \left[ \cos \frac{\pi z}{2z_q} \right]^{2\delta} & \text{if } z > z_q \\ T_a & \text{if } z \leq z_q(r). \end{cases} \quad (1.1)$$

$\delta$ , a tunable exponent controlling the rate of the disk’s vertical temperature decay, is set to 1 as in Factor et al. (2017), though it can take on values between 1-2

---

<sup>1</sup>This may or may not be a valid assumption in protoplanetary disks, but Pavlyuchenkov et al. (2007) showed that it was appropriate for CO.

(Dartois et al. 2003). The atmospheric temperature and mid-plane temperatures are given by  $T_a = T_{\text{atm},150}(r/150\text{au})^q$  and  $T_m = T_{\text{mid},150}(r/150\text{au})^q$ , where  $q$  is typically negative and controls the functions' decay. Since  $T_m$  is smaller than  $T_a$ , the second term of the low-scale height temperature function is negative, so the sinusoid effectively implements a decreasingly-negative contribution to the temperature with height above midplane. The disk's scale height, controlled by  $z_q$ , is assumed to be radially increasing, as described by a power law,  $z_q(r) = z_{q,150}(r/150\text{AU})^{1.3}$ .

The disk's velocity field is assumed to be Keplerian with slight corrections for gas pressure support and the addition of a vertical dependence. The assumption of Keplerian velocities is generally valid in the case that  $M_{\text{disk}} \ll M_{\star}$ , which continuum observations of the system have shown to be the case for these disks. With these corrections added, the model disk's velocity field is given by

$$\frac{v_{\phi}^2}{r} = \frac{GM_{\star}r}{(r+z)^{3/2}} + \frac{1}{\rho_{\text{gas}}} \frac{\partial P_{\text{gas}}}{\partial r} \quad (1.2)$$

$$v_r = v_z = 0. \quad (1.3)$$

The final structure we would like to define is the disk's gas density profile. By assuming hydrostatic equilibrium, we may relate the disk's gas density and temperature profiles as

$$-\frac{\partial \ln \rho_{\text{gas}}}{\partial z} = \frac{\partial \ln T_{\text{gas}}}{\partial z} + \frac{1}{c_s^2} \left[ \frac{GMz}{(r^2+z^2)^{3/2}} \right]. \quad (1.4)$$

Here  $c_s$  is the local sound speed, given by  $c_s^2 = \frac{k_B T_{\text{gas}}}{\mu m_H}$ ,  $T_{\text{gas}}$  is the temperature

profile given above,  $m_H$  the mass of hydrogen, and  $\mu$  is the mean molecular weight of the gas, set here at 2.37 to reflect the gas's 80% H<sub>2</sub> composition. We may solve this equation by integration, giving us the disk's density profile  $\rho(r, z)$ .

The model's surface density profile is drawn from Hartmann et al. (1998), in which they expanded on the work of Lynden-Bell & Pringle (1974) to show that the structure of an isolated disk with viscosity given by  $\nu \propto R^\gamma$  is well-described by

$$\Sigma_{\text{gas}}(r) = \frac{M_{\text{gas}}(2 - \gamma)}{2\pi R_c^2} \left(\frac{r}{R_c}\right)^{-\gamma} \exp\left[-\left(\frac{r}{R_c}\right)^{2-\gamma}\right], \quad (1.5)$$

where  $R_c$  is the radial extent of the gas disk,  $\gamma$  is a power law index, and  $M_{\text{gas}}$  is the total gas mass. This form allows the disk to behave as a power law radially until  $R_c$ , at which point it turns over into exponential decay. Hughes et al. (2008) showed that exponentially tapering the disk's outer radius, rather than sharply cutting it, provides the best agreement between gas and disk outer radii. We approximate  $M_{\text{gas}} = M_{\text{disk}}$ , since at this early stage in the disk's development, the gas is by far the majority element of the disk's mass total (although, as discussed in §???, this assumption has come under scrutiny in recent years).

Modifications are made to this density profile in two cases. At sufficiently low temperatures, molecules will condense out of the gas phase. The mid-plane of the disk is sufficiently cold to prompt this behavior. We simulate this behavior by dropping the gas density by a factor of  $10^{-18}$  wherever the temperature falls below some characteristic freeze-out temperature,  $T_{FO}$ , a temperature which is molecule-specific. Conversely, at the disk's upper surface, photodissociation by stellar and interstellar radiation dominates, so we implement a decrease in density wherever

Table 1.1: Molecule-specific values

Parameter	Description	Fixed Value(s)		
		CO, HCO <sup>+</sup>	HCO <sup>+</sup>	HCN
T <sub>FO</sub> (K)	Molecular freeze-out temperature	19	60	
σ <sub>Max</sub> (cm <sup>-2</sup> )	Column density upper limit	1.3 × 10 <sup>30</sup>	9.5 × 10 <sup>21</sup>	

\* Values drawn from Factor et al. (2017)

the hydrogen column density at the disk’s surface falls below a characteristic value. We use values drawn from Factor et al. (2017) for these parameters, presented in Table 1.1.

### 1.1.2 Generating a Model Image

Having now established our model disk’s physical structure through temperature, density, and velocity profiles, flux contributions through the disk are calculated. To do so, we find specific intensity by integrating the equation of radiative transfer:

$$I_\nu = \int_0^\infty K_\nu(s) S_\nu(s) e^{-\tau_\nu(s)} ds, \quad (1.6)$$

where  $K_\nu(s)$  is the absorption coefficient,  $\tau_\nu(s)$  is the optical depth and is defined as  $\tau_\nu(s) = \int_0^s K_\nu(s')ds'$ , and  $S_\nu(s)$  is the source function. Since disks emit as blackbodies, the Planck function,  $B_\nu(T)$ , is used as the source function. Line broadening, a function of temperature and disk turbulence, is added, and the resulting flux is Doppler shifted to account for the disk’s user-specified systemic velocity. Finally, the image is scaled, shifted, and rotated to account for the source’s distance ( $d$ ), angular offset from the center of the image ( $Δα$  and  $Δδ$ ),

and position angle and inclination (PA and  $i$ ) relative to our viewing direction.

Since the model disk is fully defined at every point in both physical and velocity space, we may set the spatial and spectral resolution to ensure that it is sampled well compared to the resolution of the data. We set our spectral resolution to match that of our observation, while we let the spatial resolution be  $\sim 1/10$  the size of the synthesized beam. This resolution is high enough to avoid sampling artifacts when we simulate interferometric observations of the image.

We then use the Miriad task `uvmodel` to generate visibilities from the model image, sampled in the same  $uv$  tracks as our observation. The  $\chi^2$  statistic is then used as a goodness-of-fit metric to compare the data and model in the visibility domain. We make this calculation in the visibility domain, rather than the image domain, so that the resulting  $\chi^2$  value is not influenced by artifacts generated in the imaging process.

In summary, we can generate a model disk by calculating its physical structures (in radial temperatures, densities, and velocities), then drawing on radiative transfer to calculate the flux contributions from the disk. That flux is sky-projected to match the observed source's orientation, and the resulting image is then transformed from the image domain to the visibility domain and its fit quality evaluated.

## 1.2 Exploring Parameter Space

Now that we have the tools available to generate synthetic images that are tunable across a large number of parameters, we must decide how best to move through that large parameter space to find a best-fit region. To do so, we use two methods.

### 1.2.1 Grid Search

The first, and perhaps most intuitive, way to move through this parameter space is using a simple grid search. A grid search involves manually assembling lists of values to try for each parameter and then generating models and calculating the resulting  $\chi^2$  value for every possible combination of parameters in those lists. A best-fit value is recovered by simply finding the point in that  $n$ -dimensional grid that yielded the best  $\chi^2$ , and then either calling that position in parameter space a best-fit location or then defining a finer grid around that point and repeating the process until an acceptable resolution has been reached. Benefits of grid search include its relatively straightforward nature (and, consequentially, the relative simplicity of implementing it) and its usefulness as a diagnostic tool, since very specific regions of parameter space may be sampled with the manual entry of positions to test. However, its simplicity leaves room for improvement.

We used grid search to locate the disks in  $(\alpha, \delta, v)$  space. All other parameters were fixed at best-guessed values, then grids were run with resolutions sufficiently fine to meet the observations' spatial and spectral resolution. Grids for the disks' systemic velocities were centered at values found in Williams et al. (2014), while  $\Delta\alpha$  and  $\Delta\delta$  offsets were first approximated using the MIRIAD task `uvfit` to fit a Gaussian to each disk. The resulting centroids were used to center the grids for refinement.

### 1.2.2 Markov Chain Monte Carlo

Markov Chain Monte Carlo (MCMC) algorithms offer us a way to both sample the probability distribution of a high-dimensional parameter space (much like a grid search), but offers an improvement over grid search by yielding the pos-

---

terior probability distribution of each point, which allows us to characterize the uncertainty associated with each best-fit value with error bars. We use an affine-invariant formulation of the MCMC algorithm described by Goodman & Weare (2010) and implemented in the Python package `emcee` by Foreman-mackey et al. (2013).

MCMC routines sample the probability distribution of a given  $n$ -dimensional parameter space by deploying an army of “walkers.” Each walker begins at some initial position, evaluates the  $\chi^2$  value of that point, and then proposes moving to a new position in parameter space according to a Gaussian probability distribution centered at the current point and decaying with distance (so that nearer points are preferentially, but not necessarily, selected). The  $\chi^2$  value of this new position - or “step” - is then evaluated, and is either accepted (the walker moves to that position) or rejected (the walker remains where it is and repeats the new-step proposal process) with probability  $p = \exp[(\chi_{\text{current}}^2 - \chi_{\text{new}}^2)/2]^2$ . This function indicates that if the proposed step yields a better fit (a lower  $\chi^2$  value) than the current position,  $p > 1$  and the step is accepted. However, if proposed step results in a worse fit, there is still a non-zero chance that the step is accepted, proportional to how much worse it is. This willingness to accept an increased  $\chi^2$  value allows the walker to avoid becoming trapped in local minima. The list of steps taken by each walker and their accompanying  $\chi^2$  values are compiled into the “chain” part of Markov Chain Monte Carlo. Goodman & Weare (2010) show that a walker’s desire to remain in near a certain position is proportional to that position’s local probability density, meaning that we may infer uncertainties in our fits from the density of walker steps taken in a region.

---

<sup>2</sup>In practice, we take the natural log of both sides of this equation, such that the quantity we are really evaluating is  $\text{lnprob} = \Delta\chi^2/2$ .

We may introduce boundaries to the parameter space explored by our walkers using “priors.” These priors are manually set, and allow us to restrict the walkers’ motions from entering regions that we know a priori to be implausible fits. Justifications for these constraints are either physical (e.g. a disk should not have a negative radius) or observed (e.g. both disks’ radii are clearly far less than 1000 AU). These priors may be either uniform, with hard cuts at their bounds (and returning  $\text{lnprob}=-\infty$ ), or Gaussian, with preferential treatment given to walkers closer to the Gaussian centroid (a known value). For this work, we implement a Gaussian prior on each disk’s position angle in order to guide the search towards the values reported in Williams et al. (2014) but still allow it the flexibility to self correct if necessary. This prior takes the form of a contribution to the log likelihood function, such that:

$$\text{lnprob} = -\chi/2 - \ln \frac{1}{\sqrt{2\pi\sigma_{PA}^2}} \exp^{-\frac{\text{PA}^2}{2\sigma_{PA}^2}} \quad (1.7)$$

for each disk’s position angle, where  $\sigma_{PA}$  is the position angle uncertainty given by Williams et al. (2014).

We may visualize the results of the walkers’ journeys using corner plots. Corner plots allow high-dimensional space to be visualized in two dimensions by taking slices across each pair of axes and showing the density of samples drawn in that slice. In each of these slices, a perfectly certain fit would appear as a very tight, point-like Gaussian - the sample density around the best fit would be extremely high and low everywhere else, as the walkers quickly converged and remained on that best fit point - while conversely, higher uncertainties are shown by a wide spread of samples around the central point. Degeneracies between parameters can

be seen as streaks in these corner plots, showing that a change in one parameter produces a change in the other. Corner plots for Disk A and B in an HCO<sup>+</sup> fit are shown in Figs 1.1a and 1.1b, respectively.

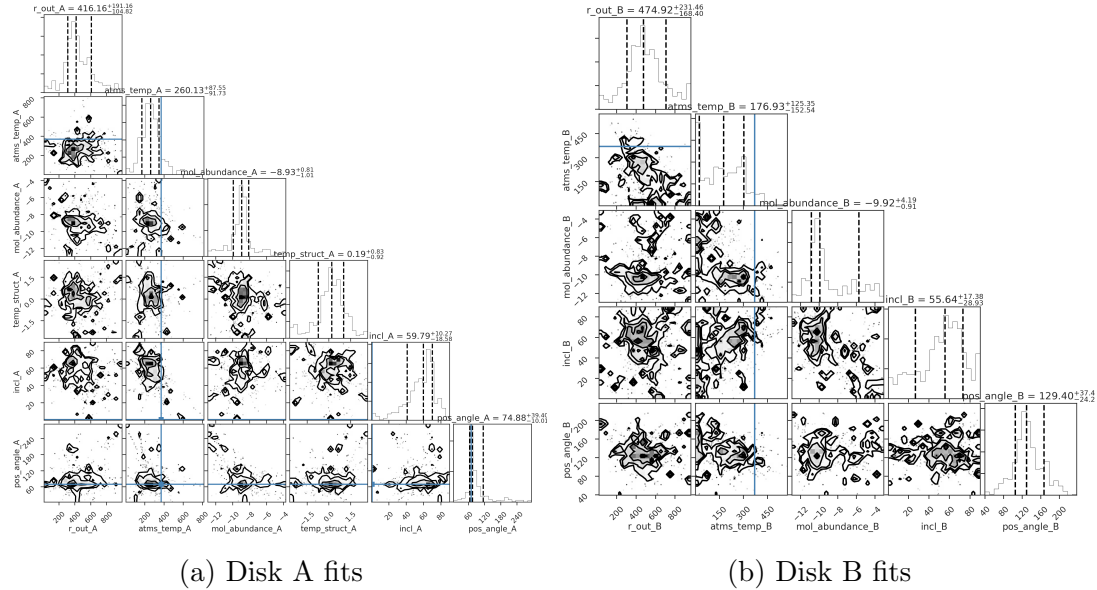


Figure 1.1: Since disk A and B's features are assumed to be independent, we may generate corner plots for each of their parameter spaces individually. Some analysis. REWORK: these are not the most recent ones

### 1.3 Fitting Procedure

Fitting of the data began with the analysis and partial removal of cloud contamination discussed in §??, resulting in the removal of baselines below a characteristic length for each line. With the data as clean as possible, position ( $\Delta\alpha, \Delta\delta$ ) and velocity ( $v_{\text{sys}}$ ) offsets were fit for. Offset fitting was executed only in the HCO<sup>+</sup> line, thanks to the line's minimal contamination and high signal strength, and was performed as described in §1.2.1. With these values established, they were treated as fixed parameters for the remainder of the fitting process.

Table 1.2 presents a list of parameters, including  $\Delta\alpha, \Delta\delta$ , and  $v_{\text{sys}}$ , which

were left fixed throughout the MCMC runs. Since we are only modeling one line at a time, we are unable to constrain the vertical temperature structure and so fix  $T_{\text{mid}}$  and  $z_q$ . The selection of  $T_{\text{mid}}$  was made following Factor et al. (2017) to reflect the “CO snow line” shown by Qi et al. (2011)<sup>3</sup>, while the value of  $z_q$  was chosen, again following Factor et al. (2017), to be roughly double the disks’ scale heights, as shown in Rosenfeld et al. (2013). Since  $\text{HCO}^+$  is optically thin, temperature and density are degenerate, so  $\gamma$  is set at 1 following Andrews et al. (2009), who showed this to be a reasonable value for disks in  $\rho$  Ophiuchus. Since our observations do not have enough spectral resolution to constrain the observations’ turbulent linewidth, we fix  $v_{\text{turb}}$  at around 1% of the sound speed, per Flaherty et al. (2015).

When fitting CO, we fix its abundance at the canonical value of  $10^{-4}$  and instead fit for disk mass. Conversely, in our fits of  $\text{HCO}^+$  and HCN emission, we fix  $M_{\text{disk}}$  at values drawn from Williams et al. (2014), which they infer from continuum flux measurements (and relying on the 100:1 gas/dust ratio discussed in §??). The remaining parameters are fit for using MCMC. We implement priors on each parameter, reported in Table 1.3. Gaussian priors are used for the fitting of both disks’ position angles, centered at values reported by Williams et al. (2014).

The results from the MCMC runs are presented below. To facilitate easier reading, accompanying figures are found at the end of the chapter.

### 1.3.1 $\text{HCO}^+$ (4-3) Fit

We began by fitting the  $\text{HCO}^+$  (4-3) line, using the MCMC methods explained above. Best fit and median values with  $1\sigma$  uncertainties are given in Table 1.4,

---

<sup>3</sup>Although their measurements were made for sources in a different environment, the value gives us a reasonable starting point for our fits.

Table 1.2: Fixed Parameter Values

Parameter	Description	Ref.	Fixed Value(s)	
			Disk A	Disk B
$\Delta\alpha$ ('')	RA offset from image center	0	0.0002	-1.006
$\Delta\delta$ ('')	Dec offset from image center	0	0.082	-0.3
$v_{\text{sys}}$ (km s <sup>-1</sup> )	Systemic velocity	0	10.00	10.75
$i$ ( $^{\circ}$ )	Inclination	1	65	45
$M_*$ ( $M_{\odot}$ )	Stellar mass	1	3.5	0.4
Log $M_{\text{disk}}$ ( $M_{\odot}$ )	Disk gas mass <sup>*</sup>	1	-1.11	-1.55
$v_{\text{turb}}$ (km s <sup>-1</sup> )	Turbulence velocity	2		0.081
$d$ (pc)	Distance	3		389
$R_c$ (au)	Critical radius	1		100
$\gamma$	Radial density power law index	4		1
$z_q$ (au)	Disk scale height at 150 AU	5		29
$T_{\text{mid}}$ (K)	Midplane temp. at 150 AU	6		19

<sup>\*</sup>  $M_{\text{disk}}$  is fixed in our fitting of HCO<sup>+</sup> and HCN, and varied for CO.<sup>0</sup> Grid-search and/or elliptical fitting, as described in §1.2.1<sup>1</sup> Williams et al. (2014)<sup>2</sup> Flaherty et al. (2015)<sup>3</sup> Gaia Collaboration et al. (2018)<sup>4</sup> Andrews et al. (2009)<sup>5</sup> Factor et al. (2017)<sup>6</sup> Qi et al. (2011)

while corner plots, showing the posterior distributions of the individual line fit, is shown in Fig. 1.3.

We see from the corner plots that, in general, the fits are quite well constrained. Uncertainties surrounding disk B's outer radius lead to some degeneracies, but overall this fit seems to be well managed. Inspection of the channel maps of the HCO<sup>+</sup> data, best-fit model, and residuals (Fig. 1.4) show that, while the model seems to reproduce the data's morphological structure fairly well, fluxes are systematically low, leaving significant residuals.

Table 1.3: Fit Parameter Values

Parameter	Description	Prior
$\log X_{\text{mol}}$	Molecular abundance, relative to $H_2$ <sup>a</sup>	Log Uniform
$q$	Radial temperature power law index	Uniform
PA (°)	Position Angle <sup>b</sup>	Gaussian
$T_{\text{atms}} \text{ (K)}$	Atmospheric temperature at 150 AU	Uniform
Log $M_{\text{Disk}} \text{ (M}_\odot\text{)}$	Disk gas mass <sup>*</sup>	Log Uniform

<sup>a</sup> For the CO line,  $X_{\text{mol}}$  is fixed at the literature value of  $10^{-4}$ .

<sup>b</sup> In our CO fit, disk B's position angle, PA, is fixed at the best-fit value from the  $HCO^+$  fits.

<sup>\*</sup> For  $HCO^+$  and HCN, disk mass was fixed at values from Williams et al. (2014).

Table 1.4: MCMC Fitting Results ( $HCO^+$ )

Parameter	Disk A		Disk B	
	Median	Best Fit	Median	Best Fit
$R_{\text{out}} \text{ (au)}$	$338.83^{+10}_{-8}$	342.22	$268.17^{+84}_{-88}$	155.48
$T_{\text{atms}} \text{ (K)}$	$221.99^{+109}_{-61}$	209.48	$182.09^{+66}_{-115}$	284.81
$X_{HCO^+}$	$-8.40^{+0.38}_{-0.24}$	-8.36	$10.32^{+0.32}_{-0.27}$	-9.91
PA (°)	$69.76^{+1.76}_{-1.24}$	70.17	$131.86^{+10.97}_{-14.35}$	120.25
$q$	$0.73^{+0.32}_{-0.47}$	0.75	[−0.5]	[−0.5]
lnprob			-28402	

\* Values in [brackets] were fixed for this run.

### 1.3.2 HCN(4-3) Fit

Next we model HCN, using the same methods as for  $HCO^+$ . As before, best fit and median values with  $1\sigma$  uncertainties are given in Table 1.5, corner plots are shown in Fig. 1.5, and channel maps are presented in Fig. 1.6.

In the channel maps, we see that the fit is generally good, leaving fairly minimal residuals behind. The residuals do, however, highlight a stream of flux connecting the two disks, particularly at velocities around  $9.4\text{-}10.2 \text{ km s}^{-1}$  that our model is

unable to fit. This stream is most visible in the HCN line, compared to the  $\text{HCO}^+$  and CO maps.

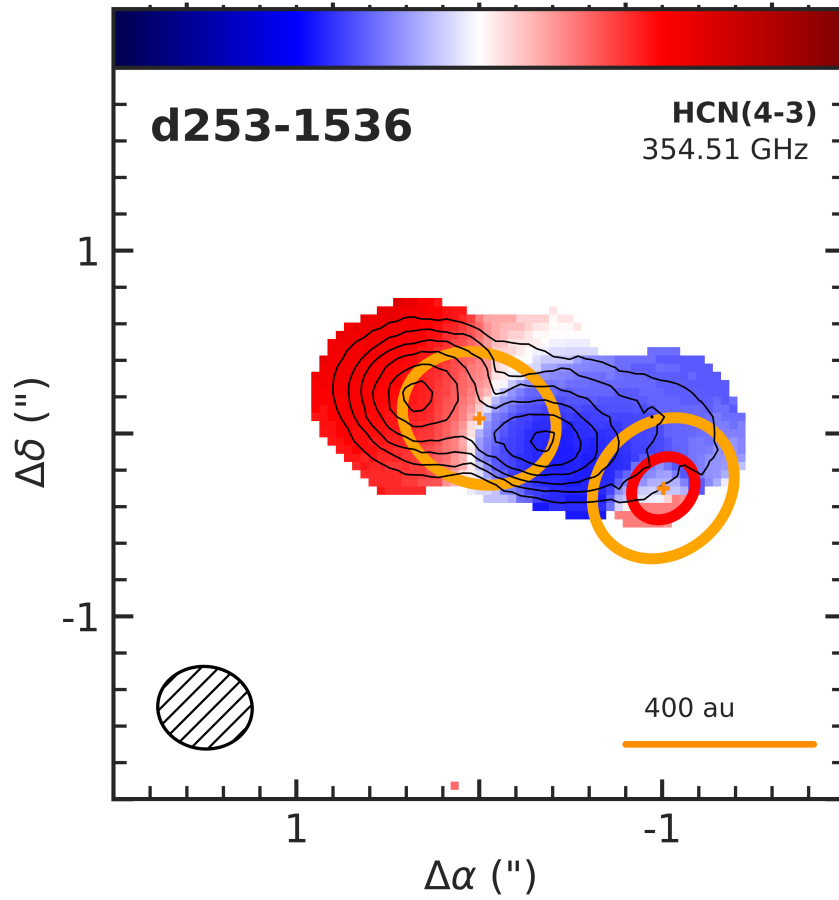


Figure 1.2: Moment-1 map of HCN emission, overlaid with ellipses described by each disk's best-fit position angle, inclination, and outer radius. For disk B, both the best-fit outer radius with and without the 220 AU *a posteriori* prior implemented (at 324 and 145 AU, respectively) are plotted.

For both disks, the posterior distribution of fits to outer radius is bimodal. This likely is a result of the MCMC walkers struggling to make sense of the above-mentioned bridge between the disks. This is particularly the case with disk B, where the walkers are distributed around 100 AU and around 350 AU. As a test,

we can remove all steps in the MCMC chain where disk B's outer radius exceeds 220 AU (which is somewhere in the middle of the bimodality in the parameter's posterior distribution, but is still appreciably higher than the HCO<sup>+</sup> fit value of  $\sim 150$  AU). Doing so brings HCO<sup>+</sup> and HCN into almost perfect agreement ( $< 1\%$ ) on disk B's outer radius, while also increasing disk A's HCN abundance by more than an order of magnitude and pushing disk B's temperature up to more than twice the value found for the HCO<sup>+</sup> line. See Table 1.6 for a selection of the fit parameters, selected based on whether they change with the radius cut. As a visual check on whether this yields a better fit, Fig 1.2 shows HCN's first moment map with both best-fit disk B radii plotted.

Otherwise, the fit's posteriors are widely unimodal and less tightly constrained than those from the HCO<sup>+</sup> fits. There are no particularly noticeable degeneracies between parameters.

Table 1.5: MCMC Fitting Results (HCN)

Parameter	Disk A		Disk B	
	Median	Best Fit	Median	Best Fit
R <sub>out</sub> (au)	448.23 <sup>+146.62</sup> <sub>-120.17</sub>	334.68	217.02 <sup>+133.53</sup> <sub>-152.70</sub>	324.50
T <sub>atms</sub> (K)	169.06 <sup>+166.57</sup> <sub>-95.87</sub>	140.95	155.78 <sup>+188.93</sup> <sub>-106.03</sub>	205.85
X <sub>HCN</sub>	-9.01 <sup>+0.89</sup> <sub>-0.55</sub>	-7.62	10.81 <sup>+0.95</sup> <sub>-1.32</sub>	-10.55
PA (°)	69.89 <sup>+1.64</sup> <sub>-1.81</sub>	69.30	-134.77 <sup>+16.15</sup> <sub>-18.61</sub>	132.22
q	0.87 <sup>+0.59</sup> <sub>-0.59</sub>	0.72	[-0.5]	[-0.5]
ln Likelihood			-30928.13	

\* Values in [brackets] were fixed for this run.

Table 1.6: HCN Fits,  $R_{\text{out}, \text{B}} < 220$ 

	$X_{\text{mol}}$	$R_{\text{out}}$ (au)	$q$	$T_{\text{atms}}$ (K)
Disk A	-6.98	337.57	0.89	86.13
Disk B	-10.3	145.57	[-0.5]	281.89

### 1.3.3 CO(3-2) Fit

Finally, we fit the CO(3-2) line. Despite the removal of baselines below  $60 \text{ k}\lambda$ , the CO(3-2) line still shows significant cloud contamination in channels near the systemic velocity (Fig. 1.8). In an attempt to keep the MCMC walkers from trying to fit the contamination, we did not evaluate the  $\chi^2$  contribution of the channels with velocities between  $9.88$  and  $12 \text{ km s}^{-1}$ , which show the worst of the clouds' effects. By choosing to not include these, we sacrifice some data, but the resulting fits are more representative of the structures we care about - the disks themselves - than they would be had we not sacrificed those channels. However, since it seems that this was insufficient, it is likely that it would have been preferable to exclude a far wider range of contaminated channels, likely from around  $6.5$  -  $13.3 \text{ km s}^{-1}$ .

Table 1.7: MCMC Fitting Results (CO)

Parameter	Disk A		Disk B	
	Median	Best Fit	Median	Best Fit
$R_{\text{out}}$ (au)	$392.66^{+0.99.21}_{-114.75}$	492.76	$199.45^{+83.34}_{-68.67}$	133.02
$T_{\text{atms}}$ (K)	$222.99^{+228.78}_{-218.54}$	2.87	$273.39^{+132.27}_{-155.72}$	473.20
$\log M_{\text{Disk}}$ ( $M_{\odot}$ )	$-2.56^{+2.03}_{-0.45}$	-0.03	$-4.76^{+0.36}_{-0.44}$	-5.18
PA (°)	$70.51^{+3.05}_{-2.71}$	72.28	[136]	[136]
$q$	$-0.03^{+0.46}_{-0.47}$	-0.03	[-0.5]	[-0.5]
ln Likelihood			-33577.41	

\* Values in [brackets] were fixed for this run.

Consequentially, the resulting fits are noticeably less certain than those of the HCO<sup>+</sup> and HCN lines, featuring several jagged and bimodal posteriors, shown in Fig.1.7. Additionally, since the best-fit values disagree significantly with the results from the other lines (particularly in the  $T_{\text{atms}}$  for disk A, which is unrealistically low), we are unable to include these results in our analysis.

Despite this, the CO line seems to have had some marginal success in recovering disk radii, returning a best-fit value disk B that is within <10% of the HCO<sup>+</sup> line's reported value, and, although the best-fit radius for disk A is unreasonably high at nearly 500 au, the model's 50<sup>th</sup> percentile fit is within 15% of the HCO<sup>+</sup> value. This seems to indicate that these data still have potential value if constrained appropriately.

Fig.1.9 show the resulting best-fit temperature and density structures in each line.

## 1.4 Reflections on the Fits

As discussed in §1.3.3, our attempts to fit the CO line were overwhelmed by the significant cloud contamination around the disk, resulting in physically-unreasonable best-fit values. If this run had converged to physical values, we would have used its disk mass results in the other runs, but since these results are not to be trusted, we instead continued to use the disks' mass values presented in Williams et al. (2014), which were inferred from continuum emission.

The HCO<sup>+</sup> and HCN runs converged into impressive agreement, although the posteriors from the HCO<sup>+</sup> line show smaller uncertainties than those of the HCN line. Both the HCO<sup>+</sup> and HCN lines show molecular abundances in disk A that are almost two orders of magnitude than those in disk B (discussed later). The

two lines' fits for disk A's outer radius agree to within around 1% (although the HCN fit is significantly less certain than the  $\text{HCO}^+$  fit) and the lines' best-fit  $q$  values agree to within 15%. Atmospheric temperatures for disk A in both lines are large and significantly different, with the  $\text{HCO}^+$  line preferring a temperature 50% greater than HCN's, but this is at least somewhat expected, as the two molecules are emitting from different regions of the disk and thus could reflect different regions of its temperature profile. In both lines, disk A's temperature structure power law index,  $q$ , is decidedly positive, although we expect this parameter to not settle with absolute certainty on a single value, since the observations don't have enough spatial resolution to constrain it tightly.

Fits for disk B are systematically less well constrained, primarily in outer radius. This likely reflects the fact that it is smaller, unresolved, and more easily overrun by emission from features that were not modeled, such as cloud contamination, excess disk A emission, and emitting material shared by the two disks. The outer radius was most notably affected by these features, yielding somewhat bimodal posteriors in both  $\text{HCO}^+$  and HCN as the walkers sometimes tried to fit the outer features. As discussed in §1.3.2, a posteriori cuts of the HCN model's MCMC chain limiting disk B's outer radius to  $\geq 220$  au - effectively manually choosing one of the posterior's two modes - changed the best-fit parameters significantly, most notably leading the HCN fit's value for disk B's outer radius into agreement with  $\text{HCO}^+$ . It also pushed disk A's HCN abundance more than a full order of magnitude higher, and into nearly perfect agreement with results from HCN fitting in Factor et al. (2017). Whether this is a reasonable thing to do is not clear to me.

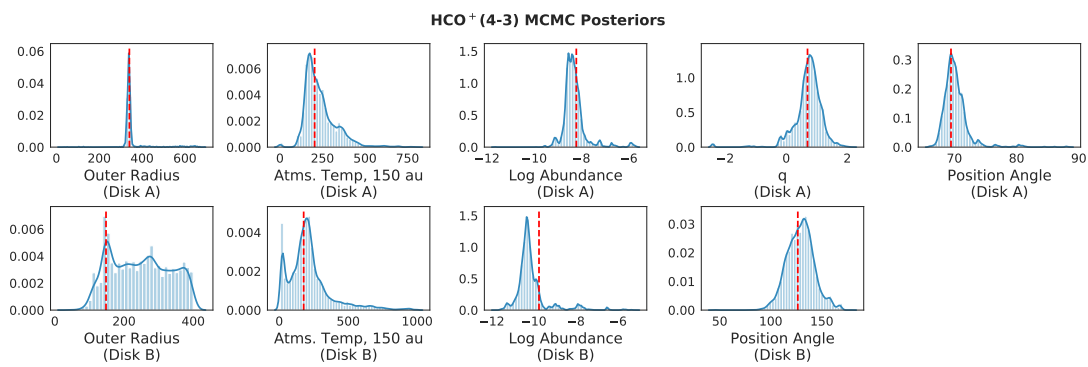


Figure 1.3: Cornerplots of results from MCMC fitting of HCO<sup>+</sup> emission.

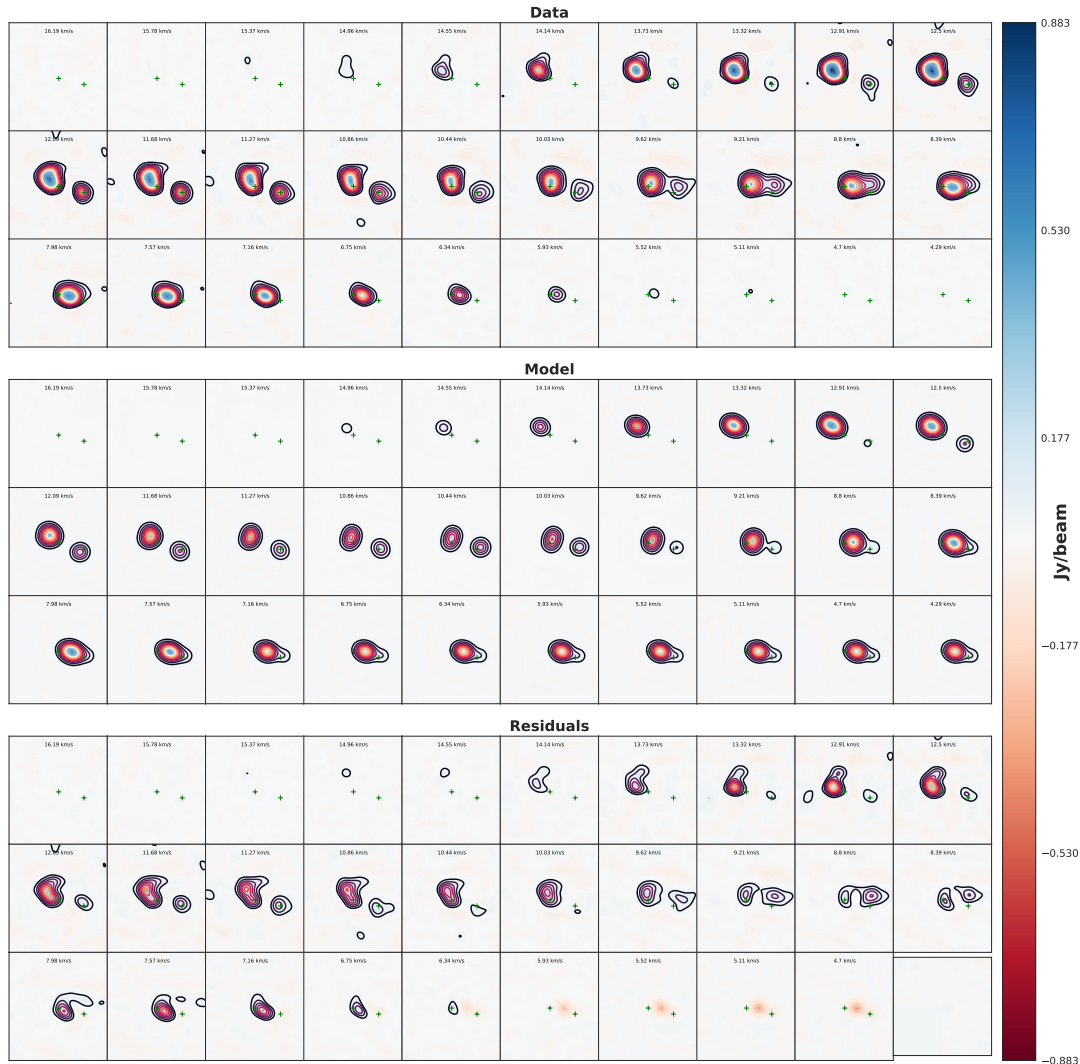


Figure 1.4: Channel maps of HCO<sup>+</sup> emission data, as well as a best-fit model from MCMC fitting and residuals from the two.

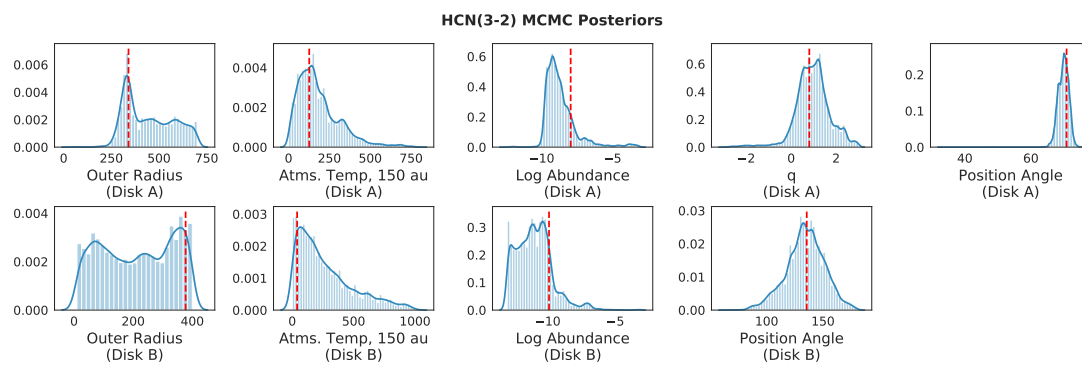


Figure 1.5: Cornerplots of results from MCMC fitting of HCN emission.

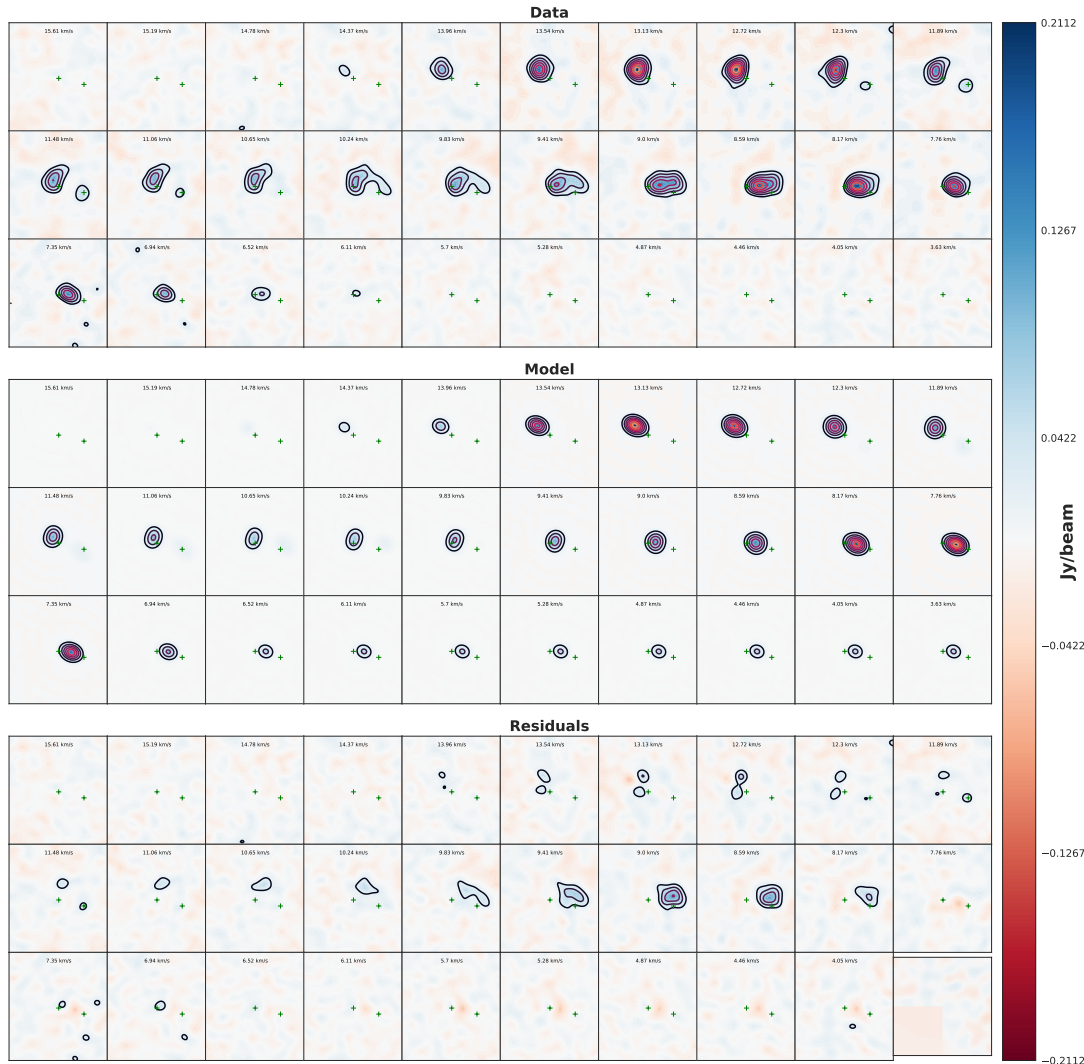


Figure 1.6: Channel maps of HCN emission data, as well as a best-fit model from MCMC fitting and residuals from the two.

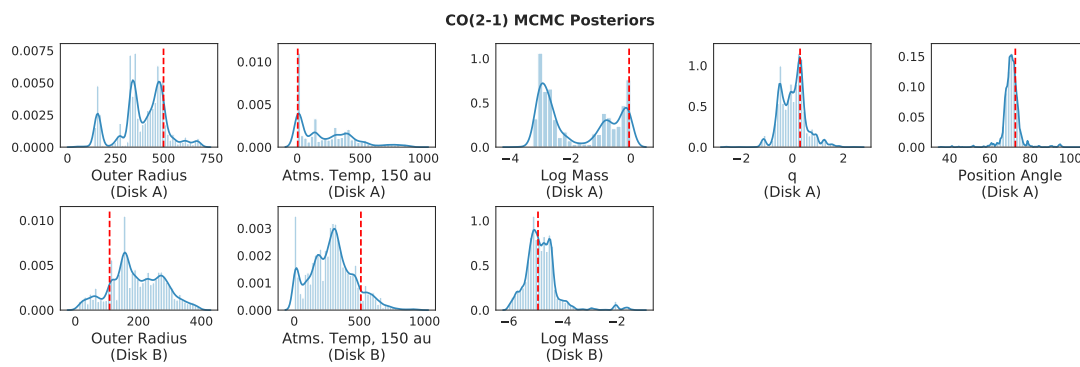


Figure 1.7: Cornerplots of results from MCMC fitting of HCN emission.

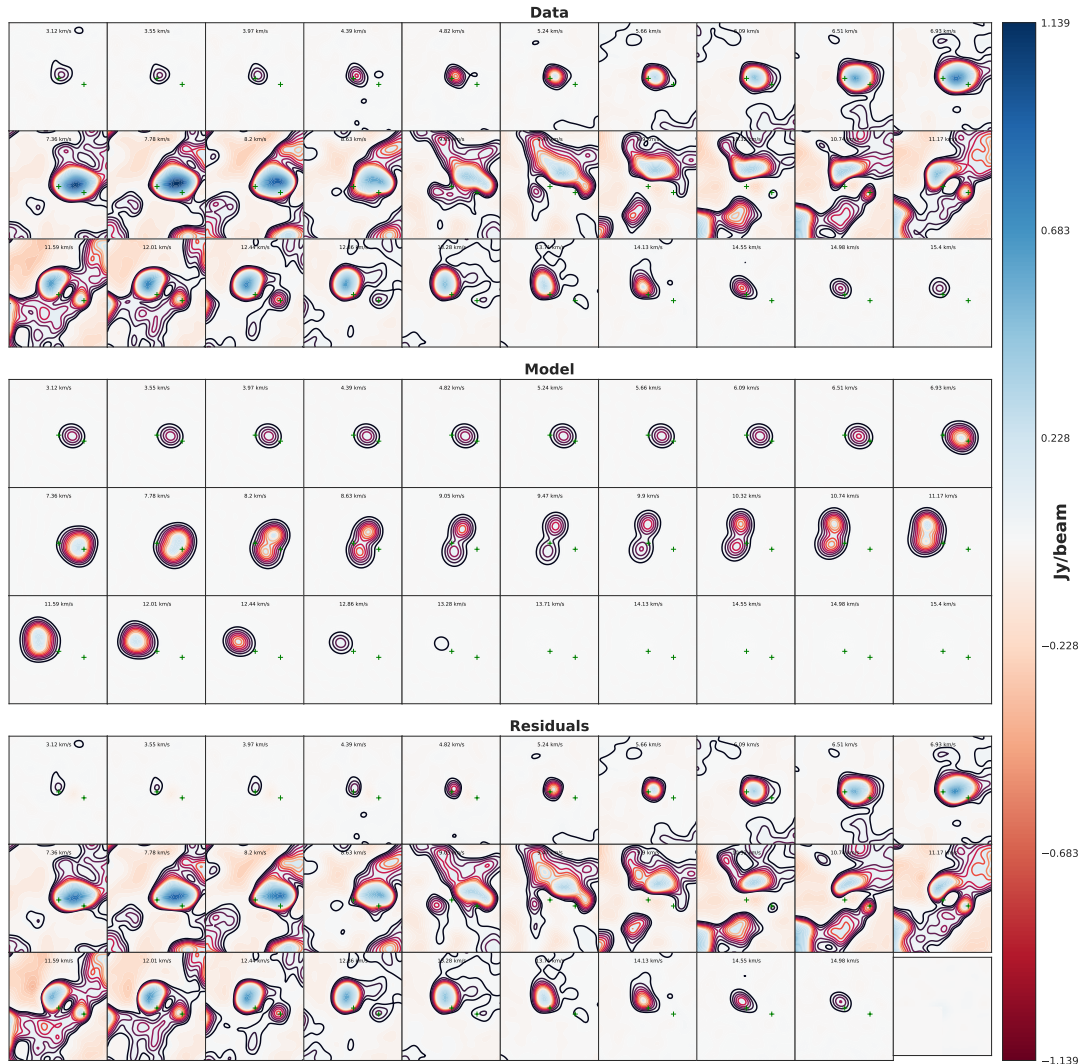


Figure 1.8: Channel maps of CO emission data, as well as a best-fit model from MCMC fitting and residuals from the two.

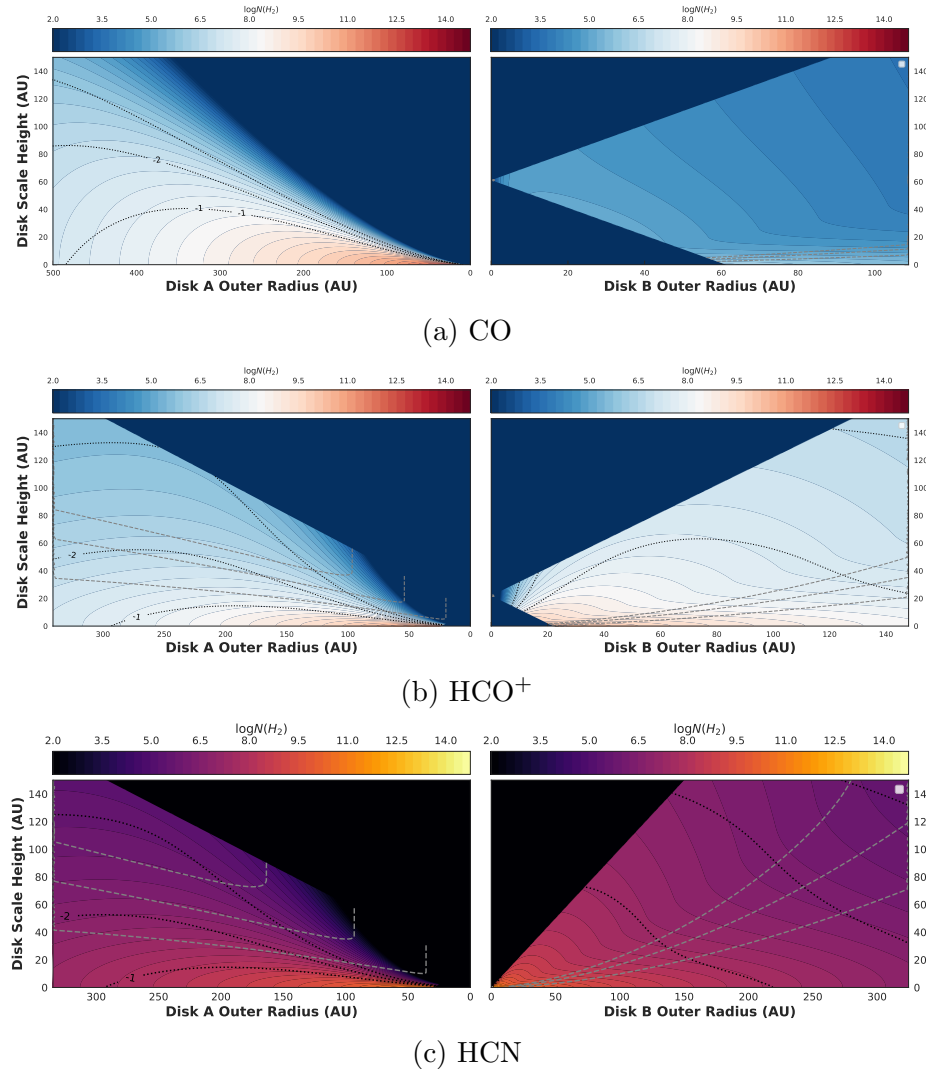


Figure 1.9: Density and temperature profiles for the best-fit models for CO,  $\text{HCO}^+$ , and HCN.

# Bibliography

- Aikawa, Y., & Herbst, E. 1999, Astron. Astrophys.
- Aikawa, Y., Umebayashi, T., Nakano, T., & Miyama, S. M. 1997, Astrophys. J., 486, L51
- . 1999, Astrophys. J., 10
- Aikawa, Y., van Zadelhoff, G. J., van Dishoeck, E. F., & Herbst, E. 2002, Astron. Astrophys., 386, 622
- Akeson, R. L., & Jensen, E. L. N. 2014, Astrophys. J., 784
- Akeson, R. L., Jensen, E. L. N., Carpenter, J., Ricci, L., Laos, S., Nogueira, N. F., & Suen-Lewis, E. M. 2019, Astrophys. J.
- Akimkin, V., Zhukovska, S., Wiebe, D., Semenov, D., Pavlyuchenkov, Y., Vasyunin, A., Birnstiel, T., & Henning, T. 2013, Astrophys. J., 766
- Anderson, K. R., Adams, F. C., & Calvet, N. 2013, Astrophys. J., 774
- Andrews, S. M., et al. 2018, Astrophys. J. Lett.
- Andrews, S. M., Rosenfeld, K. A., Kraus, A. L., & Wilner, D. J. 2013, Astrophys. J., 771
- Andrews, S. M., & Williams, J. P. 2005, Astrophys. J., 631, 1134
- . 2007, Astrophys. J., 1
- Andrews, S. M., Wilner, D. J., Hughes, A. M., Qi, C., & Dullemond, C. P. 2009, Astrophys. J., 700, 1502

- Ansdell, M., Williams, J. P., Manara, C. F., Miotello, A., Facchini, S., van der Marel, N., Testi, L., & van Dishoeck, E. F. 2017, *Astron. J.*, 153, 240
- Ansdell, M., et al. 2018, *Astrophys. J.*
- . 2016, *Astrophys. J.*
- Barenfeld, S. A., Carpenter, J. M., Sargent, A. I., Isella, A., & Ricci, L. 2017, *Astrophys. J.*, 851, 85
- Bontemps, S., et al. 2001, *Astron. Astrophys.*
- Bosman, A. D., van Dishoeck, E. F., & Walsh, C. 2018, *Astron. Astrophys.*
- Butler, B. 2012, ALMA Memo 594
- Chapillon, E. 2013, New Trends Radio Astron. ALMA Era
- Chapillon, E., Guilloteau, S., Dutrey, A., & Piétu, V. 2008, *Astron. Astrophys.*, 488, 565
- Chiang, E., & Laughlin, G. 2013, *Mon. Not. R. Astron. Soc.*, 431, 3444
- Cieza, L. A., et al. 2019, *Mon. Not. R. Astron. Soc.*, 482, 698
- Cleeves, L. I., Adams, F. C., & Bergin, E. A. 2013, *Astrophys. J.*, 772
- Cleeves, L. I., Bergin, E. A., & Adams, F. C. 2014, *Astrophys. J.*, 794
- Cleeves, L. I., Bergin, E. A., Bethell, T. J., Calvet, N., Fogel, J. K. J., Sauter, J., & Wolf, S. 2011, *Astrophys. J. Lett.*, 743, 1
- Cleeves, L. I., Bergin, E. A., Qi, C., Adams, F. C., & Öberg, K. I. 2015, *Astrophys. J.*, 799

- Collaboration, T. E. H. T. 2019, *Astrophys. J.*, 1
- Combes, F., et al. 2018, *Astron. Astrophys.*, 79, 1
- Cox, E. G., et al. 2017
- Dartois, E., Dutrey, A., & Guilloteau, S. 2003, *Astron. Astrophys.*, 399, 773
- de Gregorio-Monsalvo, I., et al. 2013, *Astron. Astrophys.*, 557, A133
- Duchêne, G., & Kraus, A. 2013, *Annu. Rev. Astron. Astrophys.*, 1
- Dullemond, C. P., & Monnier, J. D. 2010, *Annu. Rev. Astron. Astrophys.*, 1
- Dutrey, A., et al. 2014, *Nature*, 514, 600
- Dutrey, A., Guilloteau, S., & Gu, M. 1997, *Astron. Astrophys.*, 317, 55
- Eisner, J. A., et al. 2018, *Astrophys. J.*
- Eistrup, C., Walsh, C., & van Dishoeck, E. F. 2017, *Astron. Astrophys.*
- F. Shu, F. Adams, S. L. 1987, *Annu. Rev. Astron. Astrophys.*
- Factor, S. M., et al. 2017, *Astrophys. J.*
- Fatuzzo, M., & Adams, F. C. 2008, *Astrophys. J.*, 675, 1361
- Flaherty, K. M., et al. 2017, 163296, 1
- Flaherty, K. M., Hughes, A. M., Rosenfeld, K. A., Andrews, S. M., Chiang, E., Simon, J. B., Kerzner, S., & Wilner, D. J. 2015, *Astrophys. J.*, 813, 1
- Flaherty, K. M., Hughes, A. M., Teague, R., Simon, J. B., Andrews, S. M., & Wilner, D. J. 2018, 1

- Fogel, J. K., Bethell, T. J., Bergin, E. A., Calvet, N., & Semenov, D. 2011, *Astrophys. J.*, 726
- Foreman-mackey, D., Hogg, D. W., Lang, D., & Goodman, J. 2013, *Publ. Astron. Soc. Pacific*
- Gaia Collaboration. 2016, *Astron. Astrophys.*
- Gaia Collaboration, Brown, A. G. A., Vallenari, A., Prusti, T., de Bruijne, J. H. J., Babusiaux, C., & Bailer-Jones, C. A. L. 2018, *Astron. Astrophys.*
- Gaidos, E., Krot, A. N., Williams, J. P., & Raymond, S. N. 2009, *Astrophys. J.*, 696, 1854
- Goodman, J., & Weare, J. 2010, *Math. Sci. Publ.*, 5, 1
- Harris, R. J., Andrews, S. M., Wilner, D. J., & Kraus, A. L. 2012, *Astrophys. J.*, 751, 1
- Hartmann, L., Calvet, N., Gullbring, E., & D'Alessio, P. 1998, *Astrophys. J.*, 741
- Haworth, T. J., Boubert, D., Facchini, S., Bisbas, T. G., & Clarke, C. J. 2016, *Mon. Not. R. Astron. Soc.*, 463, 3616
- Henney, W. J., & O'Dell, C. R. 1999, *Astron. J.*, 118, 2350
- Henning, T., & Semenov, D. 2013
- Herrera-Martín, A., Hendry, M., Gonzalez-Morales, A. X., & Ureña-López, L. A. 2019, *Astrophys. J.*, 872, 11
- Hildebrand, R. 1983, *Q. J. R. Astron. Soc.*, 24, 267
- Hogbom, J. 1974, *Astron. Astrophys. Suppl.*

- Hubickyj, O., Bodenheimer, P., & Lissauer, J. J. 2005, Icarus, 179, 415
- Hughes, A. M. 2010, PhD thesis, Harvard University
- Hughes, A. M., Duchene, G., & Matthews, B. 2018, Annu. Rev. Astron. Astrophys., 1
- Hughes, A. M., et al. 2017, *Astrophys. J.*, 839, 86
- Hughes, A. M., Wilner, D. J., Qi, C., & Hogerheijde, M. R. 2008, *Astrophys. J.*
- Isella, A., Testi, L., Natta, A., Neri, R., Wilner, D., & Qi, C. 2007, *Astron. Astrophys.*, 469, 213
- Jensen, E. L., & Akeson, R. 2014, *Nature*, 511, 567
- Jensen, E. L. N. 1996, Phd, Arizona State University
- Johnstone, D., Hollenbach, D., & Bally, J. 1998, *Astrophys. J.*, 499, 758
- Kalyaan, A., Desch, S. J., & Monga, N. 2015, *Astrophys. J.*, 815, 112
- Kenyon, S. J., Gomez, M., & Whitney, B. A. 2008, *Handb. Star Form. Reg.* Vol. I, I
- Kraus, A. L., Ireland, M. J., Martinache, F., & Hillenbrand, L. A. 2011, *Astrophys. J.*, 731
- Kruijssen, J. M. D., & Longmore, S. N. 2019, 1
- Kuchner, M. J. 2004, *Astrophys. J.*, 612, 1147
- Lada, C. J., & Lada, E. A. 2003, Annu. Rev. Astron. Astrophys., 57
- Lai, D. 2014

- Liu, Y., et al. 2018, 75, 1
- Luhman, K. L., Allen, P. R., Espaillat, C., Hartmann, L., & Calvet, N. 2010, *Astrophys. Journal, Suppl. Ser.*, 186, 111
- Lynden-Bell, D., & Pringle, J. E. 1974, *Mon. Not. R. Astron. Soc.*, 168, 603
- Mann, R. K., Andrews, S. M., Eisner, J. A., Williams, J. P., Meyer, M. R., Di Francesco, J., Carpenter, J. M., & Johnstone, D. 2015, *Astrophys. J.*, 802, 1
- Mann, R. K., et al. 2014, *Astrophys. J.*, 784, 1
- Mann, R. K., & Williams, J. P. 2009, *Astrophys. J.*, 699, 1994
- Mansbach, P. 1970, *Astrophys. J.*
- McKee, C. F., & Ostriker, E. C. 2007, *Annu. Rev. Astron. Astrophys.*, 565
- McKinney, W. 2010, *Proc. 9th Python Sci. Conf.*, 1697900, 50
- . 2011, 19, 583
- McMullin, J. P., Waters, B., Schiebel, D., Young, W., & Golap, K. 2007, *Astron. Soc. Pacific Conf. Ser.*, 376, 127
- Miotello, A. 2017, *Proc. Int. Astron. Union*, 13, 124
- Miotello, A., Bruderer, S., & van Dishoeck, E. F. 2014, *Astron. Astrophys.*, 572, A96
- Miotello, A., van Dishoeck, E. F., Kama, M., & Bruderer, S. 2016, *Astron. Astrophys.*, 594, A85
- Observatory, A. ????, *Origins — ALMA*

- Offner, S., Kratter, K., Matzner, C., Krumholz, M., & Klein, R. 2011, Am. Astron. Soc. Meet. Abstr. 217, 43, 258
- Ovelar, M. d. J., Kruijssen, J. M. D., Bressert, E., Testi, L., Bastian, N., & Cabrera, H. C. 2012, 1, 1
- Pabst, C., et al. 2019, Disruption of the Orion molecular core 1 by wind from the massive star  $\theta$ 1 Orionis C
- Panić, O., Hogerheijde, M. R., Wilner, D., & Qi, C. 2008, Astron. Astrophys., 491, 219
- Panić, O., van Dishoeck, E. F., Hogerheijde, M. R., Belloche, A., Güsten, R., Boland, W., & Baryshev, A. 2010, Astron. Astrophys., 519, A110
- Pascucci, I., et al. 2016, Astrophys. J., 125
- Pavlyuchenkov, Y., Semenov, D., Henning, T., Guilloteau, S., Pietu, V., Launhardt, R., & Dutrey, A. 2007, Astrophys. J., 669, 1262
- Podio, L., et al. 2019, Astron. Astrophys., 6, 1
- Qi, C., D'Alessio, P., Berg, K. I., Wilner, D. J., Hughes, A. M., Andrews, S. M., & Ayala, S. 2011, Astrophys. J., 740
- Qi, C., et al. 2004, Astrophys. J., 616, L11
- Raymond, S. N., & Cossou, C. 2014, Mon. Not. R. Astron. Soc. Lett., 440
- Reboussin, L., Wakelam, V., Guilloteau, S., Hersant, F., & Dutrey, A. 2015, Astron. Astrophys., 579, A82

- Reggiani, M., Robberto, M., Da Rio, N., Meyer, M. R., Soderblom, D. R., & Ricci, L. 2011, *Astron. Astrophys.*, 534, A83
- Reipurth, B., Guimarães, M. M., Connelley, M. S., & Bally, J. 2007, *Astron. J.*, 134, 2272
- Ricci, L., Robberto, M., & Soderblom, D. R. 2008, *Astron. J.*, 136, 2136
- Ricci, L., Testi, L., Williams, J. P., Mann, R. K., & Birnstiel, T. 2011, *Astrophys. J. Lett.*, 739, 1
- Robberto, M., et al. 2013, *Astrophys. Journal, Suppl. Ser.*, 207
- Rosenfeld, K. A., Andrews, S. M., Hughes, A. M., Wilner, D. J., & Qi, C. 2013, *Astrophys. J.*, 774
- Rosenfeld, K. A., Andrews, S. M., Wilner, D. J., & Stempels, H. 2012, *Astrophys. J.*, 806
- Salyk, C., Pontoppidan, K., Corder, S., Muñoz, D., Zhang, K., & Blake, G. A. 2014, *Astrophys. J.*, 792
- Sana, H., et al. 2012, *Science (80-.)*, 337, 444
- Sault, R. J., Teuben, P. J., & Wright, M. C. H. 1995, *Astron. Data Anal. Softw. Syst.*
- Schöier, F. L., van der Tak, F. F. S., van Dishoeck, E. F., & Black, J. H. 2005, *Astron. Astrophys.*, 432, 369
- Schwarz, K. R., Bergin, E. A., Cleeves, L. I., Blake, G. A., Zhang, K., Öberg, K. I., van Dishoeck, E. F., & Qi, C. 2016, *Astrophys. J.*, 0, 1

- Skilling, J., & Bryan, R. K. 1984, Mon. Not. R. Astron. Soc., 211, 111
- Smith, N., Bally, J., Licht, D., & Walawender, J. 2005, Astron. J., 129, 382
- Tachibana, S., Huss, G. R., Kita, N. T., Shimoda, G., & Morishita, Y. 2006, Astrophys. J., 639, L87
- Tazzari, M., et al. 2017, Astron. Astrophys.
- Tripathi, A., Andrews, S. M., Birnstiel, T., & Wilner, D. J. 2017, Astrophys. J., 1
- Tsiganis, K., Gomes, R., Morbidelli, A., & Levison, H. F. 2005, Nature, 435, 459
- Van Der Walt, S., Colbert, S. C., & Varoquaux, G. 2011, Comput. Sci. Eng., 13, 22
- van Dishoeck, E. F., & Blake, G. A. 1998, Astron. Astrophys.
- Vicente, S. M., & Alves, J. 2005, in Astron. Astrophys., Vol. 205, 214–216
- Walsh, C., et al. 2016, Astrophys. J., 823, L10
- Walsh, C., Millar, T. J., & Nomura, H. 2010, Astrophys. J., 722, 1607
- . 2013, Astrophys. J. Lett., 766, 1
- Walsh, C., Nomura, H., Millar, T. J., & Aikawa, Y. 2012, Astrophys. J., 747
- Walsh, K. J., Morbidelli, A., Raymond, S. N., O'Brien, D. P., & Mandell, A. M. 2011, Nature, 475, 206
- Weidenschilling, S. 1977, Astrophys. Space Sci.
- Wernecke, S. J., & D'Addario, L. R. 1977, IEEE Trans. Signal Process., 39, 1478

- Williams, J. P., & Best, W. M. J. 2014, *Astrophys. J.*, 788
- Williams, J. P., Cieza, L., Hales, A., Ansdell, M., Ruiz-Rodriguez, D., Casassus, S., Perez, S., & Zurlo, A. 2019, *Astrophys. J. Lett.*, 1
- Williams, J. P., & Cieza, L. A. 2011, *Astrophys. J.*
- Williams, J. P., et al. 2014, *Annu. Rev. Astron. Astrophys.*, 796
- Xiao, L., & Chang, Q. 2018, *Astrophys. J.*, 853, 22
- Yu, M., Evans, N. J., Dodson-Robinson, S. E., Willacy, K., & Turner, N. J. 2017, *Astrophys. J.*, 1
- Zhang, K., Bergin, E. A., Blake, G. A., Cleeves, L. I., & Schwarz, K. R. 2017, *Nat. Astron.*, 1